



3

5

8

9

10

11

13

14

15

16

17

18

19

21

22

23

24

25

2627

Type of the Paper (Article, Review, Communication, etc.)

Intensity enhancement and *Q*-range extension in pinhole SANS instruments with neutron focusing lenses.

Aurel Radulescu 1,*

- Forschungszentrum Jülich GmbH, Jülich Centre for Neutron Science, Lichtenbergstr. 1, 85748 Garching, Germany.
- * Correspondence: a.radulescu@fz-juelich.de

Abstract: Soft matter and biological materials are characterized by a complex morphology consisting of multiple structural levels that are either hierarchically organized or coexist over a length scale from a few Å up to the size of µm. For a structural characterization of such morphologies, an extended Q range must be covered in X-ray and neutron scattering experiments. Neutrons offer the unique advantage of contrast variation and matching by D-labeling, which is of great value for the characterization of hydrocarbon systems, which are essentially the constituents of soft matter and biological materials. The combination of ultra- and small-angle neutron scattering techniques (US-ANS and SANS) on complementary beamlines has long been used for such experimental investigations. However, the combined use of USANS and SANS methods at the same beamline for simultaneous acquisition of scattering data over a wide Q-range is necessary when working with sensitive or expensive samples that require special preparation or in situ treatment during the structural characterization. For this reason, several pinhole SANS instruments have been equipped with focusing lenses to allow additional measurements at lower Q values, in the USANS range. The use of neutron lenses has the additional advantage of enhancing the intensity on the sample by providing the ability to work with larger samples while maintaining the same resolution as in pinhole mode. The experimental approach for using neutron lenses to enhance the intensity and extend the Q range to lower values than in pinhole mode is presented using examples from studies on the pinhole SANS diffractometers equipped with focusing lenses.

Keywords: SANS; USANS; neutron focusing.

Citation: To be added by editorial staff during production.

Academic Editor: Firstname Lastname

Received: date Revised: date Accepted: date Published: date



Copyright: © 2024 by the authors. Submitted for possible open access publication under the terms and conditions of the Creative Commons Attribution (CC BY) license (https://creativecommons.org/licenses/by/4.0/).

1. Introduction

Soft matter and biological systems such as polymer assemblies or blends, gels, semi-crystalline polymer membranes, polymer-protein or lipid-protein complexes are characterized by a complex morphology consisting of multiple structural levels that are either hierarchically organized or coexist over a length scale from a few Å up to the size of µm. Due to the very broad scale of relevant size levels, the experimental characterization of the structural properties of such materials under specific composition, preparation and treatment conditions is a major challenge. Scattering techniques with neutrons play an important role in such investigations [1]. Neutrons interact with matter via short-range nuclear interactions and therefore see the nuclei in a sample rather than the diffuse electron cloud observed with X-rays. The scattering length of the nuclei vary randomly in the periodic table and therefore, unlike X-rays, neutrons are able to "see" light atoms in the presence of heavier ones and distinguish neighboring elements more easily. Isotopic labeling in the labs allows neutrons to highlight structural and dynamic details in a complex multicomponent sample as neutrons can distinguish between isotopes of the same

28

29

31

32

33

34

35

36

37

38

40

41

42

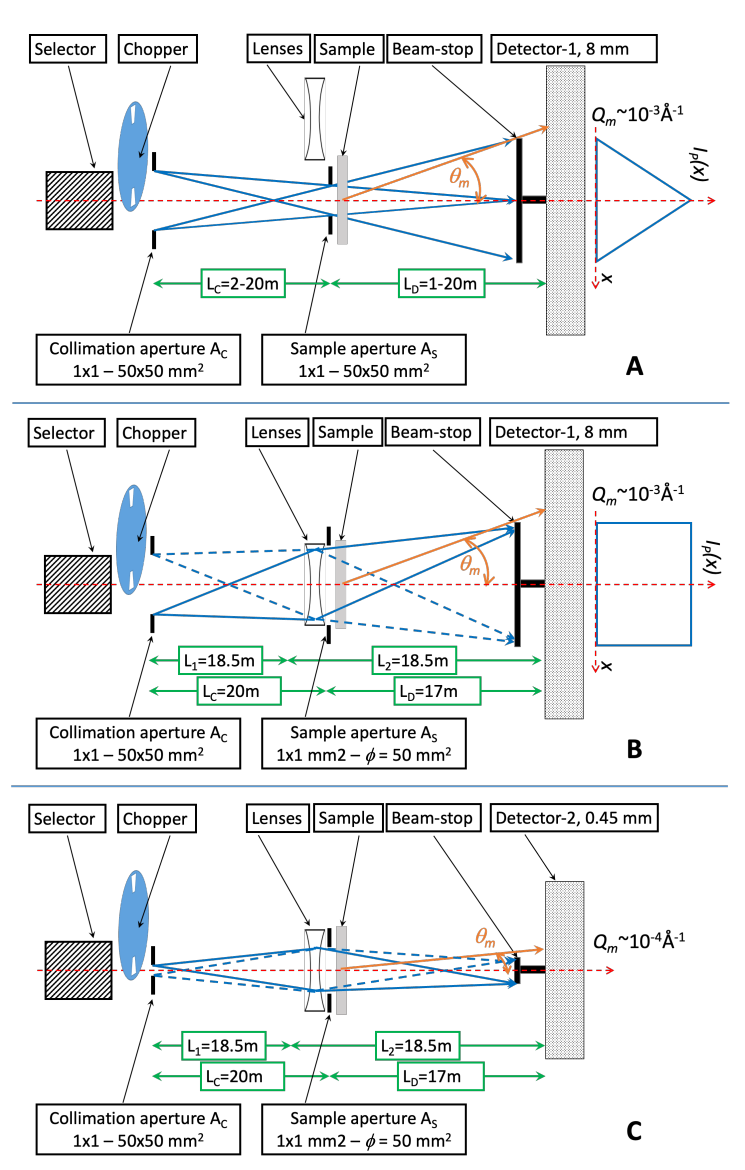


Figure 1. Schematic view of the three working modes offered for routine use of the KWS-2 SANS diffractometer of JCNS at MLZ, Germany: (A) the conventional pinhole mode; (B) the enhanced intensity focusing mode; (C) the high resolution (low *Q*) focusing mode. Reprinted (adapted) with permission from [2].

The structural features of such complex morphologies can be characterized on the mesoscale, i.e. between a few nm and 100 nm, by the small-angle neutron scattering (SANS) method. The aim of a SANS experiment is to determine the shape, size and organization of particles or aggregates dispersed in a continuous medium as a time average. Neutron scattering experiments act in reciprocal space and measure the number of neutrons scattered at different values of the momentum and energy which are transferred to the neutrons, $\hbar Q$ and $\hbar w$. Considering only the elastic scattering, the information in the SANS experiments is contained in the neutron intensity recorded on a two-dimensional position sensitive detector as a function of scattering angle θ , and which, after all corrections and calibrations related to the used method are applied, is presented as a function of the magnitude of the scattering vector Q:

67

68

69

70

71

72

73

74

75

77

78

79

81

82

83

84

85

88

91

92

93

95

96

97

98

99

100

101

102

103

104

105

106

107

109

111

112

113

114

116

117

$$Q = \frac{4\pi}{\lambda} \sin\left(\frac{\theta}{2}\right) \tag{1}$$

where λ is the wavelength of the neutron. Q acts as a kind of inverse scale: large Q values relate to short distances, while a small Q relates to large objects in real space [1]. A distinguishing feature of a SANS instrument is therefore the Q range it can cover, i.e. the scale of lengths that can be characterized with the instrument in real space.

Pinhole SANS diffractometers are the classical instruments of this type. The schematic mode of operation of such a SANS diffractometer is shown in Fig. 1A, as described in [2, 3] for the SANS diffractometer KWS-2 of the Jülich Centre of Neutron Science (JCNS) at the Heinz Maier-Leibnitz Zentrum (MLZ), Garching, Germany. A classical pinhole SANS instrument is therefore equipped with several Ac collimation apertures and one As sample aperture, each of which has a variable opening of up to several centimeters and are arranged in evacuated channels over lengths of typically 20 meters. The divergence and size of the beam on the sample to achieve the required Q resolution and hence the minimum detectable scattering angle θ_m on the detector, which can be positioned at a variable distance LD after the sample, is determined by the appropriate choice of collimation length Lc between the different Acs and the fixed position As. For Lc = LD and the optimum pinhole condition $A_C = 2A_S$, the direct beam profile I_P at the detector is approximately triangular with a base width of 2Ac. The combination of (i) a low beam divergence, i.e. the ability to detect neutrons scattered at small angles around a beam stop that masks the beam transmitted through the sample, and (ii) a relatively high beam intensity achieved by using large beam dimensions (up to several cm), in conjunction with a relatively high wavelength distribution and thus low instrumental resolution (typically $\Delta \lambda/\lambda = 10$ % as defined by the velocity selector with/without an active chopper at the entrance of the collimation system), a pinhole SANS diffractometer can cover a wide Q range by combining measurements under different λ / Lc / LD conditions [2-6]. The typical Q range for a pinhole SANS instrument, which is covered by the combination of different wavelengths λ between 3 Å and 10 Å and a detection distance L_D between 1 m and 20 m after the sample (Fig. 1A), is between 0.001 Å⁻¹ and 1.0 Å⁻¹. Longer wavelengths, up to λ = 20 Å, or a longer Lo up to 40 m are also possible, extending the Q range by a factor of 2 towards lower values, but under very demanding conditions where data quality and experiment time are strongly influenced by gravitational effects and technical requirements (detector movement, construction and maintenance costs, etc.). Therefore, structural features with sizes between a couple of nm and 100 nm are usually analyzed with a pinhole SANS instrument. To complete the structural analysis with information from the sub-nm length range and/or the large-scale range towards µm, SANS is usually combined with neutron diffraction (ND)/wide-angle neutron scattering (WANS) and ultra-SANS (USANS), which implies that different beam lines should be used in the same study.

There have been a large number of studies on soft matter and biological systems performed with USANS / SANS / ND (WANS) with extended *Q*-range combining different neutron scattering instruments, e.g. on polymers thermoreversible gels [7-11] or aerogels [12, 13], semi-crystalline polymers [1, 14-21], rubber [22-24], food [25-28] or biological systems [29-33]. However, the use of various neutron scattering methods on different beamlines also has disadvantages, which in some cases hinder optimal and reliable data acquisition, analysis and interpretation. For example, USANS, SANS and ND or WANS are not always available at the same neutron source. Furthermore, these experiments cannot always be timed closely enough to allow the same sample to be used for structural analysis over the desired broad length scale. Neutron scattering experiments are performed at large facilities that are sometimes shut down suddenly and for extended periods of time, creating additional difficulties for reliable characterization using various scattering methods on the same system. In addition, sensitive or expensive samples require special attention in sample preparation (composition, quality, quantity, etc.), preservation and transportation or on-site treatment (temperature, humidity, chemical condition, etc.) to ensure

119

120

121

122

123

124

125

126

127

128

129

130

131

132

133

134

135

136

137

138

139

140

141

142

143

144

145

146

147

148

149

151

152

153

154

155

156

157

158 159

160

161

163

165

166

167

168

169

170

reproducible sample conditions for a good performance of experiments at different beamlines. In such cases, the simultaneous use of different scattering methods at the same beamline is necessary, as has been shown in the case of using X-ray scattering methods over an extended Q range [34, 35]. Thus, in order to be able to analyze a broad size scale between one nm and one µm with the same pinhole SANS diffractometer, several such instruments have been equipped with focusing lenses [2-6, 36, 37] to allow additional measurements at lower Q values, in the USANS range, and with wide-angle detectors [38-39] to cover higher Q values, in the ND/WANS range. WANS and SANS can also be performed simultaneously, i.e. optimally and conveniently in one measurement session, with time-of-flight (TOF) SANS-diffractometers at steady state (reactors) or pulsed (spallation) neutron sources. Such instruments use a broad neutron wavelength band and a large number of detectors, either movable [40-42] or mounted at fixed positions [43-45], to simultaneously cover a large angular range in scattering and hence a wide Q range at once. Until recently, however, no TOF-SANS instrument used at research reactors or spallation sources could cover a wide Q range down to such low Q values as the pinhole SANS instruments equipped with focusing lenses and a secondary high-resolution detector (HRD). Only recently, the Multi-Slit Very Small Angle Neutron Scattering (MS-VSANS) at the China Spallation Neutron Source (CSNS), Dongguan, People's Republic of China, was put into operation [46], which resulted in the MS-VSANS instrument being able to compete with the pinhole SANS instruments with lenses in terms of achieving $Q_m \approx 0.0001$ Å⁻¹, however with complications associated with measurement in the slit geometry.

The focusing of cold neutrons with several lenses was first proposed in [47]: with biconcave MgF2 lenses, the Q range on a SANS pinhole instrument was extended down to ~ 0.004 Å-1. As described in detail in [48] the refractive index for cold neutrons is less than one, which is why neutron lenses must be concave. Several elements and isotopes suitable for neutron optics are listed in [48], where materials such as MgF₂, BeO or crystalline CO2 are discussed as potentially suitable for neutron lenses. Compared to other materials, MgF2 is relatively readily available, cheaper and easy to process. The focal length of such a lens is usually very long, about 100-200 meters. Therefore, for a SANS instrument, which typically has a detection length of 15-20 m, several such lenses should be used in series, depending on the used neutron wavelength λ . The working principle of a high resolution (low Q) focusing mode at a pinhole SANS diffractometer using lenses is shown in Fig. 1C, as operational at the KWS-2 instrument [2,3]. Generally, MgF₂ neutron lenses are focusing the image of a small entrance aperture Ac, placed on one focal point of the lens system (focusing distance L₁), on the detector that is placed on the other focal point of the lenses (focusing distance L2). Hence, working with a small entrance aperture Ac and with a high-resolution detector (HRD), neutron scattered at much lower scattering angles θ_m can be detected thus providing optimal conditions for reaching a lower value for the minimum wave vector transfer Q_m than in conventional pinhole mode. The placement of the focusing lenses in front of the sample aperture requires that for fulfilling the focusing conditions the detector should be used at slightly lower Los as in the pinhole

At this point it should be mentioned that in the 1990s reflection optics with mirrors in grazing incidence were also considered for focusing SANS instruments. However, to enable reliable measurements, a very high-quality mirror reflection surface has to be provided, which has not been achieved in most of the attempts. The only mirror-focusing SANS instrument in operation today, which complements with great success the classical pinhole SANS diffractometers with lower Q-value data, is the KWS-3 f-SANS instrument of the JCNS in Garching, Germany [49]. The instrument employs a highly polished Zerodur glass double-focusing toroidal mirror (Carl Zeiss Laser Optics GmbH, Germany) coated with 800 Å 65 Cu (refractive index for neutrons n = 0.9979 with a critical angle $\theta = 3.7^{\circ}$ for $\lambda = 12$ Å) and protected with a 100 Å Al coating, a technology developed in the 1990s for the ROSAT X-ray telescope [50]. The roughness of the mirror surface (rms) after coating is less than 3 Å. The instrument offers a successful alternative to lens focusing at

173

174

175

176

177

178

179

180

181

182

183

184

185

186

187

189

190

191

192

193

194

195

196

197

198

199

200

201

202

203

205

206

207

208

209

210

211

213

215

216

217

218

219

220

221

222

223

224

pinhole SANS diffractometers, with the advantage of avoiding gravitational effects that occur when focusing with highly chromatic lenses when a wide $\Delta\lambda/\lambda$ is used, but with disadvantages in some cases in terms of sample transmission and intensity due to the long wavelength used λ = 12 Å. Recently, the option of focusing by grazing incidence has again attracted much attention [51] by considering the use of asymmetric Wolter mirrors. Several instruments based on this principle are currently being proposed [52, 53], all of which involve the use of longer wavelengths λ than the classical pinhole SANS.

Another advantage of using neutron lenses, especially aspherical lenses to avoid geometric aberrations, was demonstrated for SANS in [54]: by using lenses, the intensity on the sample can be enhanced as a larger sample size can be used while maintaining the same resolution as the pinhole mode, as shown in Fig. 1B. The lenses should be cooled at about 77 K to increase their transmission by suppressing the phonon scattering in the lens material. By now, four pinhole SANS instruments worldwide are equipped with MgF2 lenses and a scintillation HRD based on one photomultiplier (Hammamatsu, Japan) [2-6] or ⁶LiF scintillator [37] with a resolution of ≤1 mm to make optimal use of the focusing mode for routine measurements in combination with the pinhole mode at the same beamline: KWS-2, operated by the Jülich Centre for Neutron Science at the Heinz Maier-Leibnitz Zentrum, Garching, Germany [2,3]; SANS-J, operated by the Japan Atomic Energy Agency at the JRR-3 reactor, Tokai, Japan [4,6]; SANS-U, operated by the University of Tokyo at the JRR-3 reactor, Tokai, Japan [5]; and VSANS at the National Institute of Standards and Technology (NIST, Gaithesburg, USA) [37, 55]. Only the SANS diffractometer KWS-2 [2, 3, 39] is equipped with large parabolic MgF₂ lenses (5 cm diameter) kept cold at 77K, which enable the two functions shown in Fig. 1 B and C to be routinely used with a very high profit: (i) enhancement of the intensity on the sample at the same resolution as in pinhole SANS ($Q_m \sim 10^{-3} \text{ Å}^{-1}$) using large sample sizes (up to 5 cm diameter) and (ii) extension of the Q range down to $\sim 10^{-4} \, \text{Å}^{-1}$. Three packs of lenses (4, 6 or 10 lenses) for focusing neutrons of different wavelengths when grouped together appropriately, are installed on separate carriages which can be moved in and out of the beam in a controlled manner in a special evacuated chamber in front of the sample aperture to prevent condensation of water on the lenses during cooling. Evacuation is provided by a vacuum pump that exclusively supplies the lens chamber, while cooling is provided by a cold head (VeriCold Technologies GmbH, Germany) driven by a Coolpak compressor (Leybold GmbH, Germany), with the cold being transferred to the lenses packs via cooling rails attached to the outer sides of the lenses. Nitrogen atmosphere is used to reset the chamber to room temperature and ventilate it.

In this review, the experimental approach for the use of neutron lenses to enhance the intensity and extend the *Q* range to lower values than in pinhole mode is presented using examples from studies on the SANS diffractometers KWS-2 and SANS-J [56-60].

2. Enhanced intensity using focusing lenses at pinhole SANS diffractometers

The KWS-2 SANS diffractometer is equipped with 26 MgF₂ parabolic lenses with a diameter of Φ = 5 cm. To focus monochromatic beams of different wavelength λ , as defined by the collimation aperture Ac onto the detector positioned at L_D (Fig. 1 B, C) a different number of lenses is required for different λ values. Thus, 4 lenses are used for λ = 17.5 Å, 10 lenses for λ = 10 Å and 26 lenses for λ = 7 Å. The neutron transmission of lenses is influenced by processes such as neutron absorption and scattering on the lens material. To minimize the scattering, which is mainly caused by thermal vibrations in the lens material (phonons), the lenses must be cooled to 77 K [54]. With a collimation aperture Ac of 50 mm x 50 mm at a collimation length Lc = 20 m (Fig. 1B), the lenses can focus a direct beam spot of the same size as in the pinhole SANS method (Fig. 1A) onto the main SANS detector, so that the same resolution (Q_m) as in pinhole SANS can be achieved (Fig. 1B). For an ideal focusing the condition L₁ = L₂ should be fulfilled (Fig. 1 B,C), although L₂ < L₁ may also work with the appropriate adjustment of the source image, namely the size of the collimation aperture Ac. The advantage of using this setup is that due to the possibility

229

230

231

232

233

234

235

236

237

238

239

240

241

242

243

244

245

246

247

248

249

250

251

252

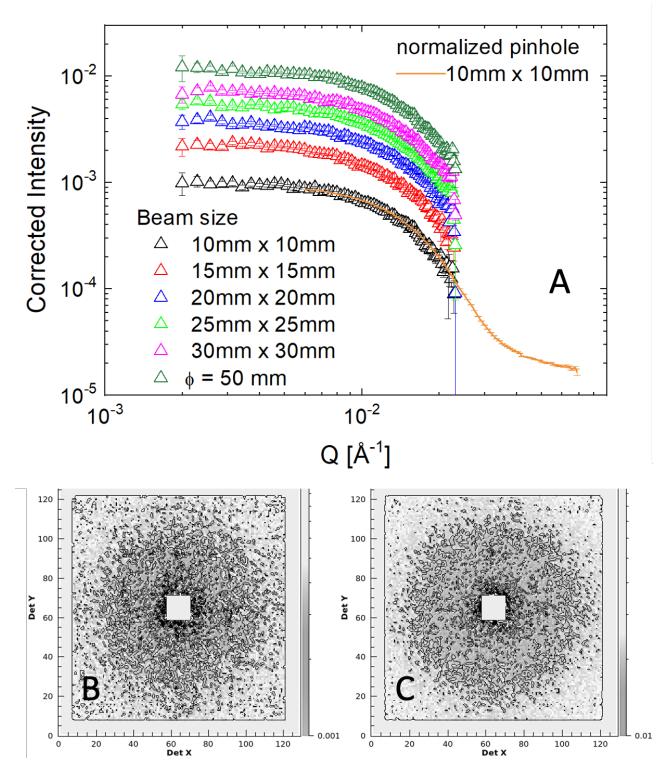


Figure 2. The scattering patterns from polystyrene particles as measured in the conventional pinhole and enhanced intensity (lenses) modes at KWS-2 [3]: the one-dimensional scattering patterns (A) and the two-dimensional scattering patterns collected on the detector in either the pinhole mode for a beam-size of $10 \text{ mm} \times 10 \text{ mm}$ (B) and the enhanced intensity mode using 26 lenses and a beam size of $30 \text{ mm} \times 30 \text{ mm}$ (C). Reprinted (adapted) with permission from [2].

Fig. 2 shows the scattering patterns of spherical polystyrene particles with a radius of R_{sph} = 150 Å in D₂O-H₂O solution, measured at KWS-2 [2] in pinhole mode with the sample aperture As size of 10 mm x 10 mm (Fig. 1A) and in the enhanced intensity mode with lenses different sample aperture size As ranging between 10 mm x 10 mm and 30 mm x 30 mm in square and a diameter of 50 mm in round shapes (Fig. 1B). Using 26 lenses with neutrons of wavelength $\lambda = 7$ Å an intensity gain on the sample of up to about twelve times is achieved by increasing the beam size on the sample (Fig. 2A), while the beam size (the Q_m resolution) on the detector remains constant, as shown in Fig. 2 B,C. The twodimensional (2D) scattering patterns (Fig. 2 B,C) are corrected for the contribution of the empty cuvette and normalized to the monitor of the incident monochromatic beam, while the one-dimensional (1D) scattering profiles (Fig. 2A) are obtained by radial averaging of the 2D scattering patterns. The intensity enhancement factor can be easily estimated by comparing the scattering levels of the plateau observed at low Q in all scattering patterns. This factor includes the transmission of the ensemble of 27 lenses kept cold at 77 K, i.e. Tr_{lenses} = 61 % when the entire lens area is used, which was estimated with the transmission monitor placed in the middle of the beam-stop [2, 3]. It should be noted that the transmission of the entire set of lenses in the cold state is about twice as high as the transmission of lenses used at RT [54], which is due to the suppression of scattering from phonons in the lens material.

254

255

256

257

258

259

260

261

262

263

264

265

266

267

268

270

271

272

273

274

275

276

277

278

279

280

281

282

283

284

285

286

287

288

289

290

291

292

Figure 3. (A) Contrast variation SANS experiments using neutron lenses in order to use larger samples of 5 cm diameter. (B) P3 amplitude (see text) versus SSE-D₂O. The minimum is found at ϕ_M = 0.61 determining the matching point. Reprinted with permission from [56]. Copyright (2014) American Chemical Society. (C) The large size (5.4 cm diameter, 1mm beam path) quartz cuvettes used with the enhanced intensity mode with lenses at KWS-2.

The use of focusing lenses to enhance the intensity on the sample by increasing the beam size on the sample, i.e. the sample size, is of great advantage for measurements at low Q on weakly scattering samples, such as in the case of very dilute particle solutions or studies of low contrast conditions or around the matching point of a labeled component in a multicomponent system by using deuterated and hydrogenated solvents in different ratios. In this case, enhancing the intensity by using larger samples helps to perform measurements with normal acquisition time and improved statistics compared to the standard setup. One should also mention that soft matter samples such as polymers, colloids, gels and some biological samples such as phospholipids are usually available in large quantities to enable such studies. One example is the study of contrast variation experiments on bovine serum albumin (BSA)-coated gold nanoparticles (GNP) exposed to simulated water effluent (SSE) to study mineralization in wastewater desalination plants [56]. 1/1 BSA-GNPs/SSE solutions with different degrees of deuteration of the SSE-D₂O content, namely 0%, 30%, 50%, 70% and 100%, were investigated. Since the particles were only stable for a short time, the weak scattering by the mineralized GNPs was overcome in the contrast variation experiment by enhancing the neutron intensity on the sample using 10 focusing lenses at KWS-2 with λ = 10 Å and a sample size of 5 cm in diameter, which allowed data acquisition of about 30 minutes with very good statistics in all contrast conditions. The corresponding data are shown in Fig. 3A, B. Analysis of the scattering patterns (Fig. 3A) resulted in a mean radius of gyration R_g of the order of 10³ Å and a Q⁻³ power law behavior of the scattering intensity at low Q. Plotting the amplitude of the power law against the SSE-D₂O content (Fig. 3B) results in a scattering minimum at 61 %, which corresponds to a matching composition of the SSE solution. It should be noted that the total scattering at the matching point is not zero, since the inner part of the particles is not homogeneous, i.e. represents a composite of BSA and GNP, as described in detail in [56].

3. Extended Q-range using focusing lenses at pinhole SANS diffractometers

Neutron lenses can be used to focus the beam transmitted through the sample to a smaller spot size and collect neutrons on an HRD, which are scattered at much smaller angles than in the classical pinhole configuration, as shown in Fig. 1C. The KWS-2, SANS-J and SANS-U diffractometers all use a scintillation detector with a single photomultiplier as HRD (Hammamatsu, Japan). Biological samples or polymer gels require special attention during preparation and treatment in the beam, where either the gelation process or the change in composition (contrast or rapid mixing of different components) must be carefully monitored.

294

295

296

297

298

299

300

301

302

303

306

307

308

309

310

311

312

313

314

315

316

317

318

319

320

321

322

323

324

325

326

327

328

329

330

331

332

333

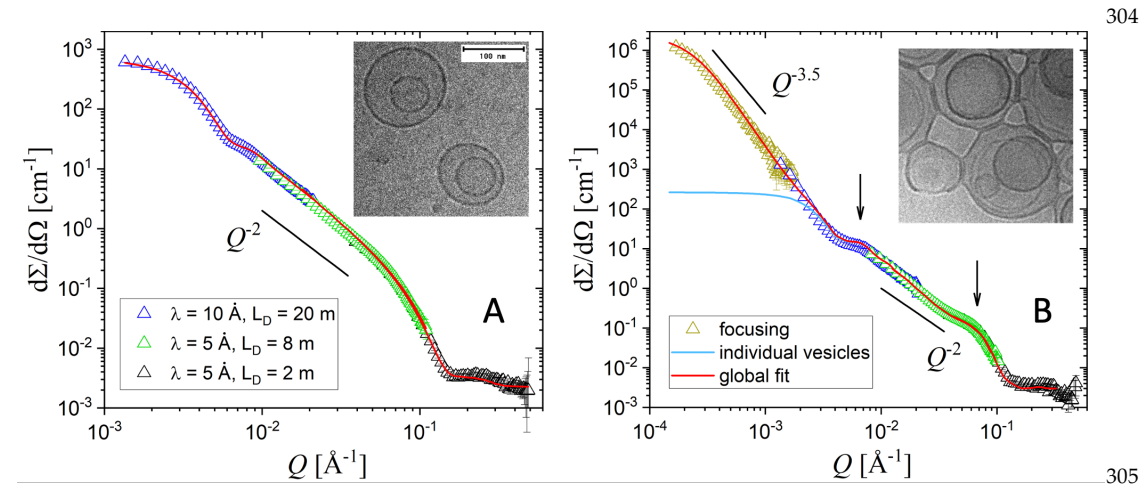


Figure 4. SANS patterns and cryo-TEM micrographs of vesicles formed by a mixture of lipids in solution without (A) and with (B) MBP addition [39]. The results of the interpretation of the scattering data according to structural models (see text) are shown by the red curves, while the signal of the docked vesicles is indicated by the light blue curve (B). The scale valid for both micrographs is 100 nm.

The myelin basic protein (MBP) and its interaction with the lipids of the myelin sheath play an important role in the pathology of multiple sclerosis (MS). The myelin sheath is a multilamellar membrane consisting of lipids and proteins that coats the axons of neurons. It plays an important role in neuronal signal conduction, as it is the insulating layer that enables rapid signal transport over long distances in the white matter of the brain by reducing conduction losses. Various diseases and conditions, such as MS, damage or destroy myelin. SANS/USANS and SAXS studies on the association of MBP with lipid membranes can shed light on the molecular origin of structure formation and structural instabilities in biosynthetic model lipid membranes with native and disease-like lipid composition and their mechanism of interaction with MBP [59, 61]. Fig. 4 A and B show scattering patterns recorded at room temperature over the entire Q range available at the KWS-2, combining the pinhole and focusing modes of a sample consisting of a mixture of lipid molecules forming unilamellar vesicles (ULV) in a D₂O buffer solution (Fig. 4A), and which exhibit adhesion (docking) effects when MBP is added to the solution (Fig. 4B), resulting in vesicle assemblies and multilamellar domains, as nicely shown in the cryo-TEM image in Fig. 4B [39]. Mixtures of lipid molecules mimicking native healthy and diseased myelin membranes were studied, with a selected case of the healthy composition study reported here. Details of the sample composition and preparation protocols can be found in [58]. Small-angle neutron scattering (SANS) was measured using the SANS diffractometer KWS-2 with conventional pinhole and high-resolution (low Q) focusing lenses modes. The experimental conditions are described in detail in [39], while in Fig. 4 A, B data measured under different λ, LD conditions or instrument operating mode are

335

336

337

338

339

340

342

344

345

346

347

349

350

351

352

353

354

355

356

357

358

359

360

361

362

363

365

367

368

369

370

371

372

373

374

375

376377

represented by different colored symbols. ULVs are formed by the mixture of lipid molecules in solution (Fig. 4A), whereby no traces of vesicle aggregation were observed even at higher lipid concentrations in the solution [59]. From the interpretation of the SANS results with the vesicle form factor (red curve in Fig. 4A), the vesicle size $R_{\text{ves}} \approx 550 \text{ Å}$ and the thickness of the bilayer $d_{ves} \approx 35$ Å were obtained. In contrast to the case of lipids alone in the solution, with MBP (Fig. 4B), the Guinier regime (the leveling off of the scattering intensity towards low Q) was observed at a Q about one order of magnitude lower compared to the protein-free solution case (Fig. 4A). The addition of MBP to the lipid solution therefore results in much larger morphologies. Additional scattering features at medium and high Q were also observed, such as the broad maxima indicated by the vertical arrows in Fig. 4B. The scattering features observed in Fig. 4B were better understood by analyzing the Cro-TEM micrographs of the same solution. The large-scale aggregates represent the vesicle assemblies mediated by the MBP, the hump at medium Q refers to the form factor detail of individual and assembled vesicles that can still be easily recognized in the micrographs, while the broad maximum at high Q is due to correlation effects caused by the local multilamellar character of the morphology where two vesicles come into contact with each other. The scattering data were well described (red curve in Fig. 4B) by a combination of single and clustering ULVs (blue line), as described in [62], combined with a Beaucage form factor [63] of the large-scale aggregates. Details of the analysis are described in [39].

The co-assembly of polyelectrolytes (PE) with proteins offers a promising approach for the development of complex structures with customizable morphology, charge distribution and stability for targeted delivery of drugs in various therapeutic applications. Such nanocarriers are fabricated from biocompatible and biodegradable materials to minimize potential toxicity and ensure safe delivery in biological systems. In [60], the morphology formed by the co-assembly of insulin/polyelectrolyte complexes and the potential for controlled release were investigated to assess their suitability for the further development of targeted drug delivery systems were studied. The complexation of insulin with a biocompatible diblock copolymer consisting of a weak polycation poly(N,N-dimethylaminoethyl methacrylate), DMA, or a strong polycation poly(N,N,N-trimethylammonioethyl methacrylate), QDMA, and a novel hydrophilic poly(ethylene oxide) block, EO, was investigated at different pH values. The detailed SANS and SAXS characterization of the complexes, complemented by cryo-TEM and a variety of laboratory analytical techniques, was reported in [60]. In D2O buffer, interconnected network-like structures of elongated and worm-like particles were formed at higher insulin concentration, as shown by USAXS and USANS. Surprisingly, only spherical or elongated particles were observed in H2O, which showed no networking behavior. This effect was attributed to the different conformational behavior of the EO block in D2O compared to H2O, which is due to the stronger hydrogen bonding between the D2O molecules and thus the weaker hydrogen bonding between EO and D₂O as well as the stronger inter- and intramolecular hydrogen bonding between the EO segments [60]. Fig. 5 shows the scattering patterns of a sample containing the diblock copolymer with a weak PE block (EO9-DMA6) at 5 mg/ml and insulin at 20 mg/ml in D₂O at pH = 7.4.

Figure 5. Scattering patterns from the complexes formed by the weakly charged diblock copolymer EO9-DMA6 and insulin in D₂O buffer at pH = 7.4, measured in enhanced intensity (yellow symbols) and extended Q-range (blue symbols) modes with lenses and SANS-J diffractometer of JAEA at JRR-3 reactor, Japan. The power law behavior of the scattered intensity in different Q ranges and the structural levels considered in the model analysis of the data are indicated. The red curve represents the global model interpretation of the experimental data, with the contribution of the large scale and mesoscale structural level depicted by the blue and black curves, respectively, as discussed in text.

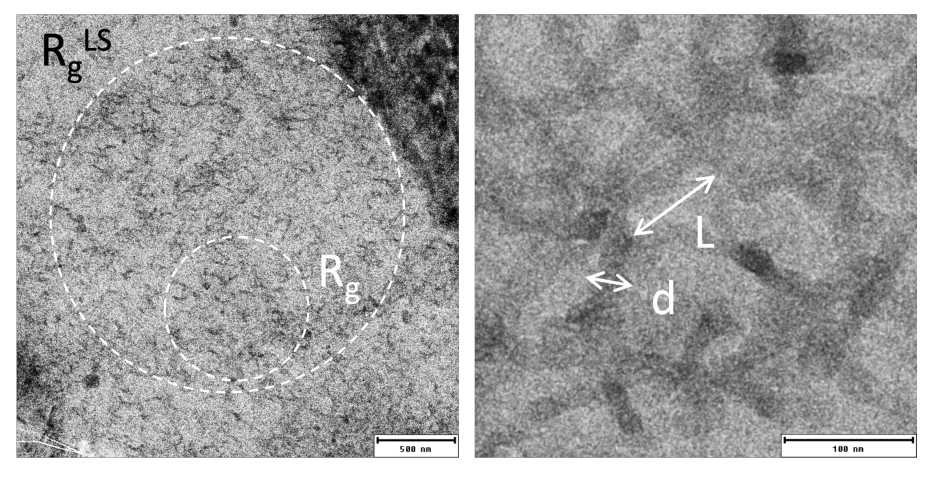


Figure 6. Cryo-TEM micrographs of the sample (EO9-DMA6) at 5 mg/ml and insulin at 20 mg/ml in D₂O buffer delivering the scattering patterns shown in Fig. 5, captured at two magnifications (scale bars 500 nm and 100 nm in the left and the right panels, respectively). The structural levels considered in the model analysis of the scattering data are indicated.

The data were collected with the SANS-J diffractometer in the Q range covered by the use of neutron lenses. The data shown with yellow symbols were measured with lenses in the enhanced intensity mode, while the scattering pattern shown with the blue symbols was collected in the USANS mode of the instrument. 70 MgF₂ with a size that allows a maximum beam size of Φ = 15 mm diameter are used on the SANS-J with λ = 6.5 Å neutrons in both enhanced intensity mode (as in Fig. 1B) and extended Q-range mode (as in Fig. 1C) [4, 6]. Thus, measurements can be performed with lenses at L_D = 10 m using the main detector [64] with an intensity gain factor of 2.7 on the sample compared to the

386

387

388

389

390

391

392

393

394

395

396

397

398

399

378

379

380

381

382

383

384

402

403

404

405

406

407

408

409

410

411

412

413

414

415

416

417

418

419

420

421

422

423

424

425

426 427

428

429

430

431

432

433

434

435

436

437

438

439

440

441

442

443

standard beam size of Φ = 8 mm used with SANS-J in pinhole mode. If a smaller collimation entrance aperture at $L_C = 10$ m is used in combination with the HRD detector at $L_D =$ 10 m, a $Q_{\rm m}$ = 0.0002 Å⁻¹ may be achieved, similar to the SANS diffractometer KWS-2. The scattering patterns in Fig. 5 exhibit varying power-law behavior at different Q scales. 1D protein-polymer complexes appear to form at the mesoscale, which behave as semi-flexible worm-like objects at a larger length scale, leading to the formation of a network-like arrangement with a mass-fractal aspect and characteristic sizes in the µm range. The main structural levels that can be identified from the change in slope observed in the scattering profile are indicated in the figure. The qualitative interpretation and model description of the scattering data in Fig. 5 are supported by cryo-TEM observations (Fig. 6), which also reveal this structural organization on a broad length scale: at µm - an ensemble of network-like assemblies (Fig. 6, left panel), consisting of associations of worm-like aggregates with sizes of several hundred nm and a local one-dimensional aspect (Fig. 6, right panel). The SANS-USANS data were modeled using the unified equation of Beaucage [63], considering three structural levels: i) the semi-flexible worm-like morphology ($\sim Q^{-5/3}$) with the size defined by the radius of gyration R_{g3} ; ii) the local 1D aspect ($\sim Q^{-1}$) of the wormlike morphologies with the characteristic sizes R_{g2} and R_{g1}; and iii) the large-scale ensemble of network-like aggregates ($\sim Q^{-3.5}$) with the characteristic size R_g^{LS} . The model interpretation describes the experimental data very well (red curve in Fig. 7) and provides the size parameters: $R_{g^{LS}}$ = 12550 \pm 125 Å, R_{g^3} = 612 \pm 15 Å, R_{g^2} = 338 \pm 16 Å and R_{g^1} = 130 \pm 10 Å. The most important structures identified and characterized by SANS are shown in Fig. 5 by the blue (large ensemble of network-forming, worm-like aggregates) and black curves (the worm-like aggregates). It should be noted that the structure levels Rg2 and Rg3 quantitatively agree quite well with the $L_{cyl} \approx 100$ nm and $d_{cyl} \approx 10$ nm estimated from the micrographs. A detailed analysis of the local scale units of this morphology at different concentration and pH conditions is reported in [60].

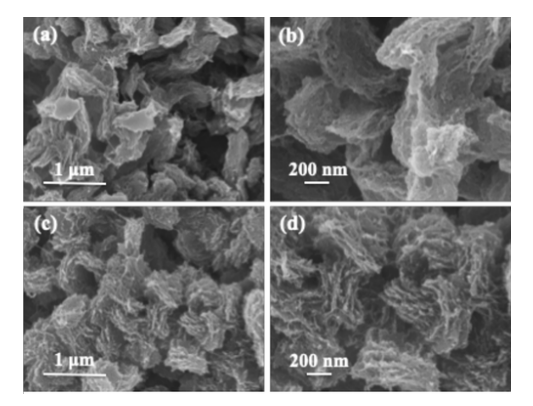


Figure 7. SEM micrographs of PEEK aerogels dried using supercritical fluid extraction. Aerogels were prepared from 15 wt % PEEK in DCA (a,b) or 4CP (c,d). Reprinted with permission from [58]. Copyright (2019) American Chemical Society.

Thermo-responsible gels of semi-crystalline polymers are characterized by three dimensional networks on a large length scale of μm size, which are formed by cross-linking smaller structural units, either crystalline lamellae or fibrils, and can include large volume fractions of solvents. The scattering patterns of such morphologies exhibit features that can be observed over an extended Q range. Thus, the crystalline peaks, which are due to ordered crystalline planes in the lamellae or fibrils, appear in the scattering patterns collected at very high Q in the ND or XRD (X-ray diffraction) regime. The lamellar or fibrillar form factors and the interlamellar or interfibrillar correlation peaks are revealed in the SANS or SAXS Q range, while the scattering profile and the Guinier regime of the large-scale associations of the lamellae or fibrils in networks can be studied with either USAXS or USANS. Highly porous aerogels, in which the morphology of the wet gel is retained,

can be produced by controlled removal of the solvent. Such aerogels are used in insulation, separation and filtration processes in many applications. A major problem in the production of aerogels is the preservation of the high porosity and the specific morphology of the wet precursor gel, which cannot be achieved by simply removing the solvent by evaporation. Therefore, the thorough characterization of the aerogels is important to evaluate the efficiency of solvent removal and the production of materials with the desired application properties.

Talley et al [58] prepared poly(ether ether ketone) aerogels after supercritical CO₂ solvent extraction (SC drying) of precursor gels prepared in either dichloroacetic acid (DCA) or 4-chlorophenol (4CP). Fig. 7 shows microscopic images of these aerogels obtained by field emission scanning electron microscopy (FE-SEM). The features of the semicrystalline morphology of the wet gels appear to be preserved, with stacked crystalline lamellae that appear to be much more defined in the SC-dried PEEK/4CP aerogels than in the SC-dried PEEK/DCA aerogels. Ultra-small angle X-ray scattering (USAXS) / small angle X-ray scattering (SAXS) / wide angle X-ray scattering (WAXS) analysis (Fig. 8A) revealed a hierarchical morphology of the PEEK aerogels with structural features ranging from PEEK crystallites to agglomerates of stacked lamellae spanning a wide range of length scales. However, SAXS cannot clearly resolve the exact nature of the structural level at the mesoscale, which appears as a broad shoulder-like scattering feature at about $Q \approx 0.04 \, \text{Å}^{-1}$.

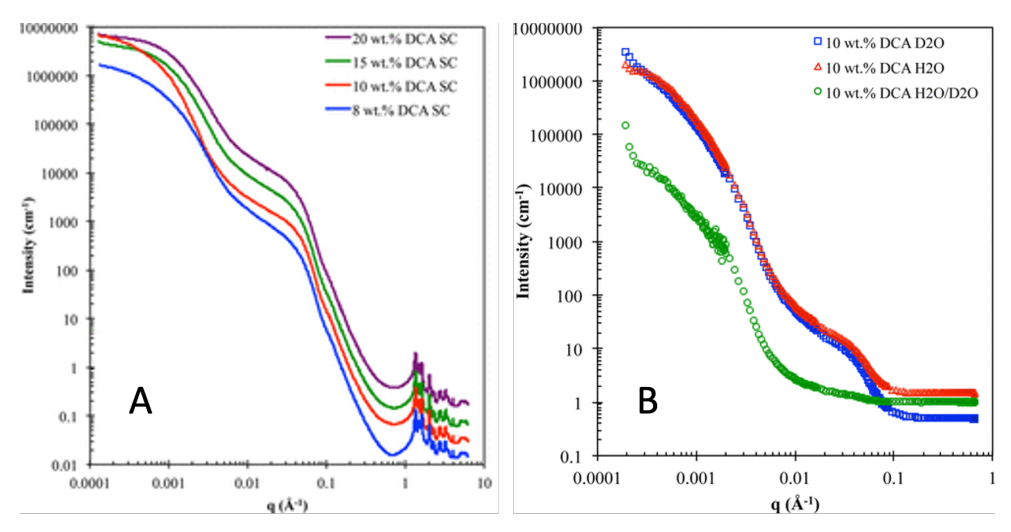


Figure 8. USAXS/SAXS/WAXS profiles of PEEK aerogels prepared by SC-drying (A) and SANS profiles of PEEK gel networks imbibed with either pure D₂O (blue squares), pure H₂O (red triangles), or 51.4:48.6 (v/v) H₂O/D₂O mixture (green circles). All gels in B were prepared via solvent-exchanging 10 wt % PEEK gels prepared in DCA. Reprinted (adapted) with permission from [58]. Copyright (2019) American Chemical Society.

SANS and USANS experiments at KWS-2, combining pinhole and high-resolution (low-Q) lenses focusing modes, provided the unique opportunity to apply contrast variations and confirmed that the morphological origin of this scattering feature of PEEK aerogels is stacked crystalline lamellae (Fig. 8B). The SANS experiments were performed on PEEK aerogels in which the DCA gelling solvent was replaced with either pure H2O, pure D2O, or a 51.4:48.6 (v/v) mixture of H2O and D2O chosen to match the scattering length density SLD of crystalline PEEK (SLD = 2.71 Å x 10^{10} cm⁻²) [58]. As noted, the broad shoulder in the SANS Q region vanishes for this contrast condition. The SANS contrast variation thus confirmed the correspondence of the scattering length density (SLD) between the liquid matrix and the crystalline PEEK lamella and provided conclusive evidence that the scattering maximum near $Q \approx 0.04$ Å⁻¹ is due to the lamellar morphology of the gels.

Kaneko et al [57] investigated the gelation of syndiotactic polystyrene (sPS) in tetrahydrofuran (THF) in the presence of high molecular weight poly(ethylene glycol) dimethyl ether (PEGDME) using contrast-matching SANS complemented by in situ FTIR. Contrast-matching SANS was used to distinguish the behavior of each polymer during the transition from the single-coil conformation at high temperature to the gel state at low temperature (10 °C), as described in detail in [57], and to be able to capture the scattering contribution of each polymer species. Therefore, each polymer species was used alternately in the deuterated state to contrast match its scattering, while the solvent always remained deuterated. After joint SANS and FTIR analysis of each sample, sPS changes from the amorphous coil conformation to the crystalline helical TTGG conformation when the gelation point is passed towards a lower temperature, forming a gel characterized by fibrillar morphologies on a mesoscale with a local 2D aspect evolving into a three-dimensional network on a large length scale. In contrast to sPS, analysis of PEGDME SANS scattering patterns collected over an extended Q range at KWS-2 down to $Q_m = 0.0002 \text{ Å}^{-1}$ and FTIR spectra showed that the PEGDME remains in amorphous conformation over the entire temperature range and transitions from the amorphous coil to an elongated amorphous conformation. It was hypothesized that this behavior is driven by the evolution of the sPS and that PEGDME integrates with the sPS into the fibrillar morphology during the gelation process.

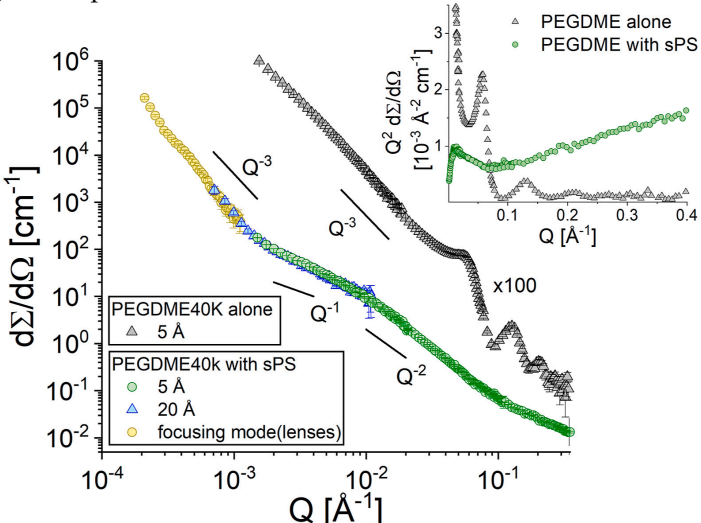


Figure 9. Scattering pattern in log-log plot from the morphology of PEGDME40K at 10°C formed as a result of the co-gelation process with the sPS in THF, measured over a wide *Q* range at matching conditions of sPS with THF (green/blue/yellow symbols). The gelation result of PEGDME40K in THF is shown in parallel in black symbols. The Kratky representation of the data is shown in the inset. The power law behavior of the scattering intensity in different *Q*-domains is given as explained in the text. Reprinted with permission from [57]. Copyright (2024) Elsevier.

The scattering pattern of PEG alone in THF solution at 10° C shows that the polymer forms a three-dimensional network of crystalline lamellae during its gelation, which resembles the morphology of a "house of cards". The interlamellar correlation peaks observed in Fig. 9, especially in the Kratky plot of the scattering data, are indicative of this morphology. Unlike this, the interpretation of the scattering patterns in the presence of sPS suggests a smaller and softer PEGDME morphology. It is clear that PEGDME follows the structural behavior of sPS and co-assembles with it to form common fibrils (Q^{-1} behavior of scattering intensity at medium Q in Fig. 9) with a localized 2D aspect (Q^{-2} profile at higher Q). In addition, the lens focusing data suggest that PEGDME is also involved in the large-scale gel structure of sPS, which leads to the stronger scattering at very low Q.

A model interpretation of the scattering pattern for medium and high *Q* values [57] in terms of a superposition of the form factor of a long and narrow parallelepiped [65]

523

524

525

526

527

528

530

531

532 533

534

535

536

537

538

539

540

541

542

543

544

545

546

547

548

549

550

551

552

553

554

555

556

557

558

559

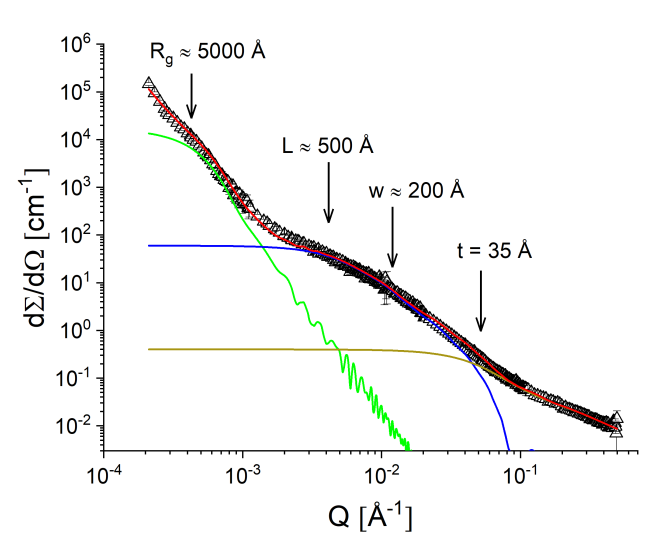


Figure 10. Model interpretation of the scattering patterns collected over an extended *Q* range at KWS-2 SANS diffractometer. The red curve depicts the global fit of the experimental data using the model discussed in text, while the green, blue and brown curves show the contribution of different structures considered in the global fit. The size levels considered in the model (see text) and the values delivered by the fit are indicated.

5. Conclusions

For a complete characterization of soft matter and biological systems a broad length scale from nm to µm should be covered in a structural analysis. This is possible with Xray and neutron scattering experiments carried out over broad Q-range. With neutrons contrast variation and matching by D-labeling is possible that is of great value for the characterization of hydrocarbon systems, which are the main constituents of soft matter and biological materials. USANS and SANS methods, sometimes complemented by ND or WANS techniques, are used for such thorough structural characterization. In the case when the sample preparation or the in-situ sample treatment during the experimental investigation pose constraints, it is useful to perform USANS and SANS experiments on the same beamline. This is possible by using pinhole SANS instruments equipped with focusing lenses that permit reaching lower Q values, in the USANS range, down to 0.0001 Å-1. The use of neutron lenses has the added benefit of increasing the intensity on the sample by providing the ability to work with larger samples while maintaining the same resolution as in pinhole mode. This is useful for measurements at low Q on weakly scattering samples, such as in the case of very dilute particle solutions or studies of low contrast conditions or around the matching point of a labeled component in a multi-component system by using deuterated and protonated solvents in different ratios. In intensity enhancement mode with focusing lenses, a significant increase in intensity on the sample is achieved depending on the size of the lenses used and the temperature of the lenses.

561 562

563

564

565

566

567

568

569

570

571

572

573

Several examples have been given to demonstrate the usefulness of using focusing lenses at pinhole SANS instruments.

Acknowledgments: Planning of, participation in and data analysis and interpretation of experiments at the small-angle neutron diffractometers KWS-2 and SANS-J by Dr. Hiroshi Nakagawa, Dr. Ryuhei Motokawa, Dr. Takayuki Kumada (all Japan Atomic Energy Agency, Japan), Dr. Dietmar Schwahn, Dr. Vitalyi Pipich, Dr. Anastasiia Murmiliuk, Dr. Benjamin Krugmann, Dr. Andreas Stadler, Dr. Maria-Maddalena Schiavone (all Forschungszentrum Jülich GmbH, Germany), Prof. Dr. Fumitoshi Kaneko (Osaka University, Japan), Dr. Samantha J. Talley and Prof. Dr. Robert B. Moore (Virginia Tech, USA) are acknowledged. Cryo-TEM observations were done in collaboration with Dr. Marie-Sousai Appavou (Forschungszentrum Jülich GmbH, Germany).

Funding: This research received no external funding.

Data Availability Statement: The data is available on request from the author.

Conflicts of Interest: The author declares no conflicts of interest.

References

575 576

1. Richter, D.; Monkenbusch, M.; Schwahn, D. Neutron Scattering. In Polymer Science: A Comprehensive Reference; Matyjaszewski, K., Möller, M., Eds.; Publisher: Elsevier Inc. Amsterdam, Netherlands, 2012; pp. 331-361.

- 2. Radulescu, A., Szekely, N. K., Appavou, M., Pipich, V., Kohnke, T., Ossovyi, V., Staringer, S., Schneider, G. J., Amann, M., Zhang-Haagen, B., Brandl, G., Drochner, M., Engels, R., Hanslik, R., Kemmerling, G. Studying Soft-matter and Biological Systems over a Wide Length-scale from Nanometer and Micrometer Sizes at the Small-angle Neutron Diffractometer KWS-2. *J. Vis. Exp.* **2016**, 118, e54639,
- 3. Radulescu, A.; Pipich, B; Frielinghaus, H.; Appavou, M-S. KWS-2, the high intensity / wide *Q*-range small-angle neutron diffractometer for soft-matter and biology at FRM II. *J.Phys.:Conf.Ser.* **2012**, *351*, 012026.
- 4. Koizumi, S.; Iwase, H.; Suzuki, J.; Oku, T.; Motokawa, R.; Sasao, H.; Tanaka, H.; Yamaguchi, D.; Shimizu, H.M.; Hashimoto, T. Focusing and polarized neutron small-angle scattering spectrometer (SANS-J-II). The challenge of observation over length scales from an ångström to a micrometre. *J.Appl.Cryst.* **2007**, 40, s474-s479.
- 5. Iwase, H.; Endo, H.; Katagiri, M.; Shibayama. M. Modernization of the small-angle neutron scattering spectrometer SANS-U by upgrade to a focusing SANS spectrometer. *J. Appl. Cryst.* **2011**, 44, 558-568.
- 6. Kumada, T.; Motokawa, R.; Oba, Y.; Nakagawa, H.; Yurina Sekine, Y.; Micheau, C.; Ueda, Y.; Sugita, T.; Birumachi, A.; Sasaki, M.; Hiroi, K.; Iwase, H. Upgrade of the small-angle neutron scattering diffractometer SANS-J at JRR-3. *J.Appl.Cryst.* **2023**, 56, 1776-1783.
- 7. Kanaya, T.; Takahashi, N.; Takeshita, H.; Ohkura, M.; Nishida, K.; Kaji, K. Structure and dynamics of poly(vinyl alcohol) gels in mixtures of dimethyl sulfoxide and water. *Polymer Journal* **2012** 44, 83–94.
- 8. Muzny, C.; de Campo, L.; Sokolova, A.; Garvey, C.J.; Rehm, C.; Hanley, H. Shear influence on colloidal cluster growth: a SANS and USANS study. *J. Appl. Cryst.* **2023**, 56, 1371-1380.
- 9. Papagiannopoulos, A.; Sentoukas, T.; Pispas, S.; Radulescu, A.; Pipich, V.; Lang, C. Length-scale dependence of pH- and temperature-response of PDMAEMA-b-PHPMA block copolymer self-assemblies in aqueous solutions. *Polymer* **2022**, 239, 124428.
- 10. Xi, Y.; Lankone, R.S.; Sung, L.-P.; Liu, Y. Tunable thermo-reversible bicontinuous nanoparticle gel driven by the binary solvent segregation. *Nat.Commun.* **2021**, 12, 910.
- 11. Tirumala, V.R.; Tominaga, T.; Lee, S.; Butler, P.D.; Lin, E.K.; Gong, J.P.; Wu, W. Molecular Model for Toughening in Double-Network Hydrogels. *J. Phys. Chem. B* **2008**, 112, 8024-8031.
- 12. Leventis, N.; Sotiriou-Leventis, C.; Chandrasekaran, N.; Mulik, S.; Larimore, Z.J.; Lu, H.; Churu, G.; Mang, J.T. Multifunctional Polyurea Aerogels from Isocyanates and Water. A Structure-Property Case Study. *Chem. Mater.* **2010**, 22, 6692–6710.
- 13. Tran, T.S.; Balu, R.; Mata, J.; Dutta, N.K.; Choudhury, N.R. 3D printed graphene aerogels using conductive nanofibrillar network formulation. *Nano Trends* **2023**, *2*, 100011.
- 14. Radulescu, A.; Goerigk, G.; Fetters, L.J.; Richter, D. Morphology of crystalline–amorphous olefin block copolymers in solution characterized by small-angle neutron scattering and microscopy. *J.Appl.Cryst.* **2015**, 48, 1860-1869.
- 15. Yuzhan Li, Y.; Keum, J.K.; Wang, J.; Naisheng J.; Bras, W.; Kessler, M.R.; Rios, O. Multiscale Structural Characterization of a Smectic Liquid Crystalline Elastomer upon Mechanical Deformation Using Neutron Scattering. *Macromolecules* **2021**, 54, 22, 10574–10582.
- 16. Kim, M-H.; Glinka, C.J.; Grot, S.A.; Grot, W.G. SANS Study of the Effects of Water Vapor Sorption on the Nanoscale Structure of Perfluorinated Sulfonic Acid (NAFION) Membranes. *Macromolecules* **2006**, 39, 14, 4775–4787.

574

577 578 579

7s- 580 7is. 581 582 iif- 583

584 co, T. 585 ngth 586

596 - 597 598

595

599 600

601 602

603

605 606 n 607

> 609 610 611

608

- 17. Kanaya, T.; Matsuba, G.; Ogino, Y.; Nishida, K.; Shimizu, H.M.; Shinohara, T.; Oku, T.; Suzuki, J.; Otomo, T. Hierarchic Structure of Shish-Kebab by Neutron Scattering in a Wide Q Range. *Macromolecules* **2007**, 40, 3650-3654.
- 18. Kim, M-H.; Glinka, C.J. Correlation between Structure and Vapor Sorption in Semicrystalline Linear Polyethylene: One Dimensional Nano-Swelling Measured Using in Situ Vapor Sorption Small Angle Neutron Scattering (iVSANS). *Macromolecules* **2009**, 42, 7, 2618–2625.
- 19. Lund, R.; Alegria, A.; Goitandia, L.; Colmenero, J.; Gonzalez, M.A.; Lindner, L. Dynamical and Structural Aspects of the Cold Crystallization of Poly(dimethylsiloxane) (PDMS). *Macromolecules* **2008**, 41, 1364-1376.
- 20. Motokawa, R.; Iida, Y.; Zhao, Y.; Hashimoto, T.; Koizumi, S. Living Polymerization Induced Macro- and Microdomain Investigated by Focusing Ultra-small-angle Neutron Scattering. *Polymer Journal* **2007**, 39, 1312–1318.
- 21. Koizumi, S.; , Zhao, Y.; Putra, A. Hierarchical structure of microbial cellulose and marvelous water uptake, T investigated by combining neutron scattering instruments at research reactor JRR-3, Tokai. *Polymer* **2019**, 176, 244–255.
- 22. Takenaka, M.; Nishitsuji, S.; Watanabe, Y.; Yamaguchi, D.; Koizumi, S. Analyses of hierarchical structures in vulcanized SBR rubber by using contrast-variation USANS and SANS. *J. Appl. Cryst.* **2021**, 54, 949–956.
- 23. Koga, T.; Hashimoto, T.; Takenaka, M.; Aizawa, K.; Amino, N.; Nakamura, M.; Yamaguchi, D.; Koizumi, S. New insight into hierarchical structures of carbon black dispersed in polymer matrices: a combined small-angle scattering study. *Macromolecules* **2008**, 41, 453-464.
- 24. Yamaguchi, D.; Yuasa, T.; Sone, T.; Tominaga, T.; Noda, Y.; Koizumi, S.; Hashimoto, T. Hierarchically Self-Organized Dissipative Structures of Filler Particles in Poly(styrene-ran-butadiene) Rubbers. *Macromolecules* **2017**, 50, 7739–7759.
- 25. Callaghan-Patrachar, N.; Peyronel, F.; Pink, D.A.; Marangoni, A.G.; Adams. C.P. USANS and SANS investigations on the coagulation of commercial bovine milk: Microstructures induced by calf and fungal rennet. *Food Hydrocolloids* **2021**, 116, 106622.
- 26. Bayrak, M.; Mata, J.; Conn, C.; Floury, J.; Logan, A. Application of small angle scattering (SAS) in structural characterisation of casein and casein-based products during digestion. *Food Research International* **2023**, 169, 112810.
- 27. Gilbert, E.P. Neutron Techniques for Food Colloids. Current Opinion in Colloid & Interface Science 2023, 67, 101730
- 28. Smith, G.N. Revisiting neutron scattering data from deuterated milk. Food Hydrocolloids 2021, 113, 106511
- 29. Pencer, J.; Jackson, A.; Kucerka, N.; Nieh, M-P.; Katsaras, J. The influence of curvature on membrane domains. *Eur. Biophys. J.* **2008**, 37, 665-671.
- 30. Greene, D.G.; Modla, S.; Wagner, N.J.; Sandler, S.I.; Lenhoff, A.M. Local Crystalline Structure in an Amorphous Protein Dense Phase. *Biophysical Journal* **2015**, 109, 1716–1723.
- 31. Iashina, E.G.; Bouwman, W.G.; Duif, C.P.; Dalgliesh, R.; Varfolomeeva, E.Y.; Pantina, R.A.; Kovalev, R.A.; Fedorova, N.D., Grigoriev, S.V. Time-of-flight spin-echo small-angle neutron scattering applied to biological cell nuclei. *J. Appl. Cryst.* **2023**, 56, 1512-1521.
- 32. Mangiapia, G.; Gvaramia, M.; Kuhrts, L.; Teixeira, J.; Koutsioubas, A.; Soltwedel, O.; Frielinghaus, H. Effect of benzocaine and propranolol on phospholipid-based bilayers. *Phys. Chem. Chem. Phys.* **2017**, 19, 32057-32071.
- 33. Xiao, Y.; Liu, Q.; Clulow, A.J.; Li, T.; Manohar, M.; Gilbert, E.P.; de Campo, L.; Hawley, A.; Boyd, B.J. PEGylation and surface functionalization of liposomes containing drug nanocrystals for cell-targeted delivery. *Colloids and Surfaces B: Biointerfaces* **2019**, 182, 110362.
- 34. Tashiro, K., Sasaki, S. Structural changes in the ordering process of polymers as studied by an organized combination of the various measurement techniques. *Polymer* **2003** 28, 451–519.
- 35. Pauw, B. R.; Smith, A. J.; Snow, T.; Shebanova, O.; Sutter, J. P.; Ilavsky, J.; Hermida-Merino, D.; Smales, G. J.; Terrill, N. J.; Thünemann, A. F.; Bras, W. Extending synchrotron SAXS instrument ranges through addition of a portable, inexpensive USAXS module with vertical rotation axes. *J. Synchrotron Rad.* **2021**, 28, 824–833.
- 36. Wood, K.; Mata, J. P.; Garvey, C. J.; Wu, C.-M.; Hamilton, W. A.; Abbeywick, P.; Bartlett, D.; Bartsch, F.; Baxter, P.; Booth, N.; Brown, W.; Christoforidis, J.; Clowes, D.; d'Adam, T.; Darmann, F.; Deura, M.; Harrison, S.; Hauser, N.; Horton, G.; Federici, D.; Franceschini, F.; Hanson, P.; Imamovic, E.; Imperia, P.; Jones, M.; Kennedy, S.; Kim, S.; Lam, T.; Lee, W. T.; Lesha, M.; Mannicke, D.; Noakes, T.; Olsen, S. R.; Osborn, J. C.; Penny, D.; Perry, M.; Pullen, S. A.; Robinson, R. A.; Schulz, J. C.; Xiong, N.; Gilbert, E. P. QUOKKA, the pinhole small-angle neutron scattering instrument at the OPAL Research Reactor, Australia: design, performance, operation and scientific highlights. *J. Appl. Cryst.* 2018, 51, 294–314.
- 37. Barker, J.; Moyer, J.; Kline, S.; Jensen, G.; Cook, J.; Gagnon, C.; Kelley, E.; Chabot, J. P.; Maliszewskyj, N.; Parikh, C.; Chen, W.; Murphy, R. P.; Glinka, C. The very small angle neutron scattering instrument at the National Institute of Standards and Technology. *J. Appl. Cryst.* **2022**, 55, 271–283.
- 38. Heller, W. T.; Cuneo, M.; Debeer-Schmitt, L.; Do, C.; He, L.; Heroux, L.; Littrell, K.; Pingali, S. V.; Qian, S.; Stanley, C.; Urban, V. S.; Wu, B.; Bras, W. The suite of small-angle neutron scattering instruments at Oak Ridge National Laboratory. *J. Appl. Cryst.* 2018, 51, 242–248.
- Radulescu, A.; Kang, J-J.; Appavou, M-S.; Papagiannopoulos, A. Upgrade of JCNS SANS instrument KWS-2 for improved performance and beam-time efficiency. EPJ Web of Conferences 2023, 286, 03006.
- 40. Heenan, R. K.; King, S. M.; Turner, D. S.; Treadgold, J. R. (2005). ICANS-XVII. 17th Meeting of the International Collaboration on Advanced Neutron Sources, 25–29 April 2005, Santa Fe, New Mexico, USA.

- 41. Zhao, J. K.; Gao, C. Y.; Liu, D. The extended *Q*-range small-angle neutron scattering diffractometer at the SNS. *J. Appl. Cryst.* **2010**, 43, 1068–1077.
- 42. Sokolova, A.; Whitten, A.E.; de Campo, L.; Christoforidis, J.; Eltobaji, A.; Barnes, J.; Darmann, F.; Berry, A. Performance and characteristics of the BILBY time-of-flight small-angle neutron scattering instrument. *J. Appl. Cryst.* **2019**, 52, 1-12
- 43. Takata, S.; Suzuki, J.; Shinohara, T.; Oku, T.; Tominaga, T.; Ohishi. K.; Iwase, H.; Nakatani, T.; Inamura, Y.; Ito, T.; Suzuya, K.; Aizawa, K.; Arai, M.; Otomo, T.; Sugiyama, M. The Design and q Resolution of the Small and Wide Angle Neutron Scattering Instrument (TAIKAN) in J-PARC. *JPS Conf. Proc.* **2014**, 8, 036020.
- 44. Koizumi, S.; Noda, Y.; Maeda, T.; Inada, T.; Ueda, S.; Fujisawa, T.; Izunome, H.; Robinson, R. A.; Frielinghaus, H. Advanced Small-Angle Scattering Instrument Available in the Tokyo Area. Time-Of-Flight, Small-Angle Neutron Scattering Developed on the iMATERIA Diffractometer at the High Intensity Pulsed Neutron Source J-PARC. *QuBS*, **2020**, *4*, 42.
- 45. Allen, A. J. J. Appl. Cryst. 2023, 56, 787–800.
- 46. Zuo, T.; Han, Z.; Ma, C.; Xiao, S.; Lin, X.; Li, Y.; Wang, F.; He, Y.; He, Z.; Zhang, J.; Wang, G.; Cheng, H. The multi-slit very small angle neutron scattering instrument at the China Spallation Neutron Source. *J. Appl. Cryst.* **2024**, 57, 380–391.
- 47. Choi, S-M.; Barker, J.G.; Glinka, C.J.; Cheng, Y.T.; Gammel, P.L. Focusing cold neutrons with multiple biconcave lenses for small-angle neutron scattering. *J. Appl. Cryst.* **2000**, 33, 793-796.
- 48. Eskildsen, M.R.; Gammel, P.L.; Isaacs, E.D.; Detlefs, C.; Mortensen K.; Bishop, D.J. Compound refractive optics for imaging and focusing of low-energy neutrons. *Nature* **1998**, 391, 563-566.
- 49. Goerigk, G.; Varga, Z. Comprehensive upgrade of the high-resolution small-angle neutron scattering instrument KWS-3 at FRM II. *J. Appl. Cryst.* **2011**, 44, 337-342.
- 50. Alefeld, B.; Dohmen, L. Richter, D.; Brückel, T. Space technology from X-ray telescopes for focusing SANS and reflectometry. *Physica B* **2000**, 276-278, 52-54.
- 51. Liu, D.; Gubarev, M.V.; Resta, G.; Ramsey, B.D.; Moncton, D.E.; Khaykovich, B. Axisymmetric grazing-incidence focusing optics for small-angle neutron scattering. *Nucl. Inst. Meth. A.* **2012**, 686, 145-150.
- 52. Wu, H.; Hong, W.; Zhang, Y.; Bai, P.; Mo, W.; Yang, Y.; Gong, H.; Zhang, Z.; Xu, X.; Cai, W.; Wang, P.; Wang, Z.; Wang, X. Conceptual design of the grazing-incidence focusing small-angle neutron scattering (gif-SANS) instrument at CPHS. *J. Neutron Res.* **2021**, 23, 201-205.
- 53. Samothrakitis, S.; Bertelsen, M.; Willendrup, P.K.; Knudsen, E.B.; Larsen, C.B.; Rizzi, N.; Zanini, L.; Santoro, V.; Strobl, M. Neutron instrument concepts for a high intensity moderator at the European spallation source. *Sci. Rep.* **2024**, 14, 9360.
- 54. Frielinghaus, H.; Pipich, V.; Radulescu, A.; Heiderich, M.; Hanslik, R.; Dahlhoff, K.; Iwase, H.; Koizumi, S.; Schwahn, D. Aspherical refractive lenses for small-angle neutron scattering. *J. Appl. Cryst.* **2009**, 42, 681–690.
- 55. Barker, J.G. Methods to maximize detector count rates on small-angle neutron scattering diffractometers at reactor sources: II. Optimizing sample, source and detector sizes. *Nucl. Inst. Meth. A.* **2024**, 1059, 168973.
- 56. Dahdal, Y.N.; Pipich, V.; Rapaport, H.; Oren, Y.; Kasher, R.; Schwahn, D. Small-Angle Neutron Scattering Studies of Mineralization on BSA Coated Citrate Capped Gold Nanoparticles Used as a Model Surface for Membrane Scaling in RO Wastewater Desalination. *Langmuir* 2014, 30, 15072–15082.
- 57. Kaneko, K.; Schiavone, M-M.; Iwase, H.; Takata, A.; Allgaier, J.; Radulescu, A. Microstructural investigation of the cooperative gelation of syndiotactic polystyrene and high M_W polyethylene glycol di-methyl ether in common solution in THF. *Polymer* **2024**, 12677
- 58. Talley, S.J.; Vivod, S.L.; Nguyen, B.A.; Meador, MA.N.; Radulescu, A.; Moore, R.B. Hierarchical Morphology of Poly(ether ether ketone) Aerogels. *ACS Appl. Mater. Interfaces* **2019**, 11, 31508–31519.
- 59. Krugmann, B.; Radulescu, A.; Appavou, M-S.; Koutsioubas, A.; Stingaciu, L.R.; Dulle, M.; Förster, S.; Stadler, A.M. Membrane stiffness and myelin basic protein binding strength as molecular origin of multiple sclerosis. *Scientific Reports* **2020**, 10, 16691.
- 60. Murmiliuk, A.; Iwase, H.; Kang, J-J.; Mohanakumar, S.; Appavou, M-S.; Wood, K.; Almasy, L.; Len, A.; Schwärzer, K.; Allgaier, J.; Dulle, M.; Gensch, T.; Förster, B.; Ito, K.; Nakagawa, H.; Wiegand, S.; Förster, S.; Radulescu, A. Polyelectrolyte-protein synergism: pH-responsive polyelectrolyte/insulin complexes as versatile carriers for targeted protein and drug delivery. *J.Coll.Interface Sci.* **2024**, 665, 801–813.
- 61. Raasakka, A.; Ruskamo, S.; Kowal, J.; Barker, R.; Baumann, A.; Martel, A.; Tuusa, J.; Myllykoski, M.; Bürck, J.; Ulrich, A.S.; Stahlberg, H.; Kursula, P. Membrane Association Landscape of Myelin Basic Protein Portrays Formation of the Myelin Major Dense Line. *Scientific Reports* 2017, 7, 4974.
- 62. Komorowski, K.; Salditt, A.; Xu, Y.; Yavuz, H.; Brennich, M.; Jahn, R.; Salditt, T. Vesicle Adhesion and Fusion Studied by Small-Angle X-Ray Scattering. *Biophysical Journal* **2018**, 114, 1908–1920.
- 63. Hammouda, B. Analysis of the Beaucage Model. J. Appl. Cryst. 2010, 43, 1474–1478
- 64. Noda, Y.; Koizumi, S.; Yamaguchi, D. Multi-tube area detector developed for reactor small-angle neutron scattering spectrometer SANS-J-II. *J. Appl. Cryst.* **2016**, 49, 128-138.
- 65. Pedersen, J. S. Analysis of small-angle scattering data from colloids and polymer solutions: modeling and least-squares fitting. *Adv. Colloid Interface Sci.* **1997**, 70, 171-210.

- 66. Beuacage, G.; Rane, S.; Sukumaran, S.; Satkowski, M.M.; Schechtman, L.A. Persistence length of isotactic poly (hydroxy butyrate). *Macromolecules*, **1997**, 30, 4158-416.
- 67. Papagiannopoulos, A. Chapter 10 Small Angle Neutron Scattering (SANS). In Microscopy Methods in Nanomaterials Characterization; Thomas, S., Thomas, R., Zachariah, A.J., Mishra, R.K., Eds.; Publisher: Elsevier Inc. Amsterdam, Netherlands, 2017; pp. 339-361.

732

728